

1 **Characterizing the Composition of Sand and Mud Suspensions**
2 **in Coastal & Estuarine Environments using Combined Optical**
3 **and Acoustic Measurements**

4 **Stuart G. Pearson^{1,2}, Romaric Verney³, Bram C. van Prooijen¹, Duc Tran³, Erik C.M.**
5 **Hendricks^{1,2}, Matthias Jacquet³, and Zheng Bing Wang^{2,1}**

6 ¹Faculty of Civil Engineering and Geosciences, Delft University of Technology, PO Box 5048, 2600GA Delft, the

7 Netherlands

8 ²Deltares, P.O. Box 177, 2600MH Delft, the Netherlands

9 ³IFREMER, 1625 Route de Sainte-Anne, 29280 PlouzanÃI, France

10 **Key Points:**

- 11 • Suspended sand and mud can be distinguished by their different optical and acous-
12 tic backscatter signatures
- 13 • We define a sediment composition index (SCI) from relative optical and acoustic
14 backscatter and verify it with lab and field measurements
- 15 • SCI can be used to estimate the fraction of suspended sand, adding interpretive
16 value to measurements in mixed sediment environments

Abstract

Quantifying and characterizing suspended sediment is essential to successful monitoring and management of estuaries and coastal environments. To quantify suspended sediment, optical and acoustic backscatter instruments are often used. Optical backscatter systems are more sensitive to fine particles ($< 63\mu\text{m}$) and flocs, whereas acoustic backscatter systems are more responsive to larger sand grains ($> 63\mu\text{m}$). It is thus challenging to estimate the relative proportion of sand or mud in environments where both types of sediment are present. The suspended sediment concentration measured by these devices depends on the composition of that sediment, so it is also difficult to measure concentration with a single instrument when the composition varies. The objective of this paper is to develop a methodology for characterizing the relative proportions of sand and mud in mixed sediment suspensions by comparing the response of simultaneous optical and acoustic measurements. We derive a sediment composition index (SCI) that can be used to directly predict the relative fraction of sand in suspension. Here we verify the theoretical response of these optical and acoustic instruments in laboratory experiments, and successfully apply this approach to field measurements on the ebb-tidal delta of Ameland Inlet in the Netherlands. Increasing sand content decreases SCI, which was verified in laboratory experiments. A reduction in SCI is seen under more energetic conditions when sand resuspension is expected. Conversely, the SCI increases in calmer conditions when sand settles out, leaving behind finer sediment. This approach provides crucial knowledge of suspended sediment composition in mixed sediment environments.

Plain Language Summary

Sand and mud particles are the building blocks of our coastlines. Counting and describing sand and mud particles floating through the water is essential to managing coasts. We commonly do this with devices that send out a sound (acoustic) or light (optical) signal into the water. The sensors measure the strength of the signal reflecting back off of any sand and mud particles passing by. Optical instruments are better at “seeing” mud than sand, and acoustic instruments are better at “hearing” sand than mud. If both sand and mud are present, a single instrument will not accurately estimate the total amount of sediment because of these different sensitivities. Instead, we can use both types of instrument together and compare what we “see” with what we “hear”. This comparison allows us to estimate whether there are more sand or mud particles floating through the water. The

49 relationship between “seeing” and “hearing” can be described in a single number, the sed-
50 iment composition index (*SCI*). We successfully tested this approach in laboratory experi-
51 ments and then applied it to a site on the coast of the Netherlands. This approach gives us
52 a new way to understand environments that are both sandy and muddy.

53 **1 Introduction**

54 **1.1 Background**

55 Estuaries and coastal seas are characterized by strong morphological and sedimen-
56 tary gradients, from shallow beaches and intertidal shoals or flats, to deeper foreshore
57 and channel areas or other subtidal features. Furthermore, the sediment composition at
58 a given site may vary widely in both particle size and mineralogy [*Winkelmolen and Veen-*
59 *stra, 1974; Flemming and Ziegler, 1995; Son et al., 2011*]. The size and material proper-
60 ties of fine sediment (a.k.a. “fines” or “mud”) and sand are different: sand particles are
61 individual quasi-spherical grains (with typical density $\rho_s = 2,650\text{kg/m}^3$ for quartz par-
62 ticles), between 63 and $2,000\mu\text{m}$ in diameter, d . Fine sediments, especially clay particles
63 ($d < 2\mu\text{m}$), have the ability to flocculate and often bond with organic matter. The result-
64 ing flocs vary widely in diameter (from 10 to $1,000\mu\text{m}$) and have relatively low densities
65 ($\rho_{floc} = O(1, 100 - 2,000\text{kg/m}^3)$) with irregular shapes and lower settling velocities than
66 sand [*Chapalain et al., 2019; Many et al., 2019*]. The spatial distribution of these different
67 types of sediment is a function of morphology, supply, and hydrodynamic conditions.

68 Due to episodic (storms and floods) and persistent (tides) hydro-meteorological forc-
69 ing and human influences, estuarine and coastal sediment are highly dynamic. Bed sedi-
70 ments are mobilized and transported, through bed load (rolling, sliding, and saltating near
71 the surface of the seabed) or suspended load (held aloft in the water column by turbu-
72 lence). In this paper we focus on transport in suspension, dealing with fine sediments or
73 mud ($d < 63\mu\text{m}$) and very fine to medium sand $d = 63 - 500\mu\text{m}$, the latter being found
74 in suspension (relatively close to the bed) during energetic conditions. Depending on local
75 and remote bed composition and hydrodynamic forcing, the concentration and nature of
76 suspended particulate matter (SPM) will drastically change.

77 The main challenge faced in understanding coastal sediment dynamics and quanti-
78 fying associated fluxes is thus to make continuous observations of total (sand and mud)
79 suspended sediment and their related mass concentration (*SSC*). Continuous *in situ* mea-

80 measurements are possible with acoustic or optical instruments [Fettweis *et al.*, 2019], but their
 81 measurement capabilities are inextricably tied to the material properties of the sediment
 82 they observe. Each type of instrument responds with different sensitivity to fine or sandy
 83 sediment because of a dependence on particle size and density. Hence, in practice, cali-
 84 bration models for optical or acoustic sensors are built against *in situ* samples, the latter
 85 providing reference gravimetric concentration. However, these models are representative
 86 of a given condition (e.g., calm, moderate tidal flows with SPM dominated by fine sedi-
 87 ments), and are not well-adapted for observing a succession of low- and high-energy con-
 88 ditions when the SPM sand and mud content (f_{sand} and f_{mud}) can vary strongly in time.
 89 The most appropriate methodology would require sampling and re-calibrating sensors as
 90 fast as SPM composition changes, but this is neither easily predictable nor realistic. A li-
 91 brary of population-adapted calibration models could be built following *Green and Boon*
 92 [1993], but knowledge about SPM composition dynamics is a prerequisite for their appli-
 93 cation.

94 In this context, we propose an original sediment composition index (*SCI*) derived
 95 from optical and acoustic measurements to quantitatively and dynamically evaluate the
 96 relative fraction of sand or fine sediments in suspension. The concept is first validated
 97 using laboratory measurements, and then applied to field measurements.

98 1.2 Optical Backscatter Measurements

99 Optical Backscatter (OBS) sensors are widely used to indirectly measure suspended
 100 sediment concentration. Near-infrared light (typical wavelength $\lambda = 0.780 - 0.865\mu m$) is
 101 emitted from the instrument, backscattered by suspended particles, and then recorded by
 102 photoreceptors. In a Mie scattering regime, backscatter is strongest when the light wave-
 103 length and particle size are similar, so OBS are more sensitive to fine sediment particles
 104 $O(1\mu m)$ than sand particles $O(100\mu m)$ [Green and Boon, 1993; Conner and De Visser,
 105 1992; Voulgaris and Meyers, 2004]. According to Sutherland *et al.* [2000], the photon flux
 106 received by the sensor is given as:

$$107 \quad F = VNE \frac{\pi d^2}{4} Q_s \quad (1)$$

108 Where F is photon flux [W], V is scattering volume [cm^3], N is the number con-
 109 centration of scatters [cm^{-3}], E emitted irradiance [W/cm^2], d is the particle diameter
 110 [μm], Q_s the (back)scattering efficiency of the particles [-]. Relating the number concen-
 111 tration to the mass concentration SSC [mg/L], this relationship can be modified as follows
 112 [*Sutherland et al.*, 2000]:

$$113 \quad F = \frac{3}{2} \frac{V(SSC)E}{\rho_s d} Q_s \quad (2)$$

114 Where ρ_s is the particle (dry) density [kg/m^3]. This flux is then translated to a volt-
 115 age output by the sensor.

116 Equation 2 can then be reworked as:

$$117 \quad OBS = \alpha_{OBS} \frac{Q_s}{\rho_s d} SSC \quad (3)$$

118 Where OBS is the optical backscatter signal [V] and α_{OBS} is approximated as a
 119 constant for the range of SSC investigated.

120 Due to the dependency on $1/(\rho_s d)$, for the same concentration of sediment, the flux
 121 observed for $200\mu m$ sand ($\rho_s \approx 2600kg/m^3$) will be 10 times smaller than for flocs of the
 122 same size ($\rho_{floc} \approx 1100kg/m^3$), and even smaller in presence of microflocs.

123 **1.3 Acoustic Backscatter Measurements**

124 Analogously to OBS devices, an acoustic signal is emitted and backscattered by par-
 125 ticles in suspension, then recorded by transducers. The estimation of SSC from acoustic
 126 measurements depends on the properties of sediment in suspension. For well-characterized
 127 particles (e.g., a well-sorted sand population) and electronically/acoustically calibrated
 128 sensors, backscattering models and representative diameters can be used to evaluate SSC
 129 from the theory [*Thorne and Hanes*, 2002]. Otherwise, similarly to optical sensors, the
 130 acoustic response can be calibrated against samples from field or laboratory experiments,
 131 with similar limitations regarding calibration representativity.

132 Acoustic devices typically used in coastal sediment studies can loosely be grouped
 133 into (i) single-frequency Acoustic Doppler Velocimeters (ADV) which measure at a sin-

134 gle point; (ii) single-frequency Acoustic Doppler Current Profilers (ADCPs) which mea-
 135 sure over multiple points in the water column; and (iii) multi-frequency acoustic backscat-
 136 ter devices. Only the latter is specifically designed to measure suspended sediment con-
 137 centration; ADCPs and ADVs were originally intended to measure velocity, but their op-
 138 erating principles mean that inferring sediment concentration from acoustic backscat-
 139 ter is a useful side benefit. In this study, we mainly consider acoustic backscatter from
 140 ADVs, which are widely used to measure suspended sediment concentrations [*Fugate and*
 141 *Friedrichs, 2002; Öztürk, 2017; Lin et al., 2020*].

142 We can mathematically describe acoustic backscatter using the sonar equation, which
 143 balances the difference between energy emitted and received by the sensor with energy
 144 lost on the return trip of an acoustic pulse [*Hoitink and Hoekstra, 2005*]. The sonar equa-
 145 tion is presented here in form similar to [*Hoitink and Hoekstra, 2005; Salehi and Strom,*
 146 *2011; Chmiel et al., 2018*]:

$$147 \quad SNR = C - \underbrace{20 \log_{10}(\psi R^2)}_{\text{Spherical Spreading}} - \underbrace{\int_0^R (\alpha_w(r) + \alpha_s(r)) dr}_{\text{Attenuation}} + BI \quad (4)$$

148 SNR [dB] is the Signal-to-Noise Ratio recorded directly by the ADV, which in-
 149 dicates the intensity of acoustic backscatter. C [dB] is a constant including instrument-
 150 related and geometrical terms. The spherical spreading term ($20 \log_{10}(\psi R^2)$) is a function
 151 of R [m], the one-way distance that the acoustic pulse travels from the transmitter to the
 152 measurement volume. The attenuation of the acoustic pulse can be decomposed into ab-
 153 sorption by the water α_w [dB/m] and attenuation by sediment α_s [dB/m], integrated over
 154 the travel distance. BI is the volume backscatter strength [dB] and is a function of SSC
 155 and particle characteristics:

$$156 \quad BI = 10 \log_{10} \left(\frac{SSC \bar{\sigma}}{\rho_s \bar{V}_s} \right) \quad (5)$$

157 Where $\bar{\sigma}$ is the mean backscattering cross section [m^2], ρ_s is the dry particle den-
 158 sity [kg/m^3], and \bar{V}_s is the scattering volume [m^3].

159 The attenuation terms (α_s and α_w) are higher at larger concentrations and greater
 160 distances [*Thorne et al., 1993*], but can be neglected below 1,000mg/L [*Chmiel et al.,*

161 2018] and $O(10\text{cm})$ from the sensor [Pomázi and Baranya, 2020]. In this study we thus
 162 neglect attenuation, given the small distance between source and measuring volume (15
 163 cm) and low concentrations expected at our study site in Ameland ($< 1,000\text{mg/L}$). All
 164 terms except BI can be reorganized and set in a global constant C' [dB]. Equation 5 then
 165 becomes:

$$166 \quad SNR = 10 \log_{10}(SSC) + 10 \log_{10} \left(\frac{\bar{\sigma}}{\rho_s \bar{v}_s} \right) + C' \quad (6)$$

167 Equation 6 can be further simplified as:

$$168 \quad SNR = 10 \log_{10}(SSC) + b' + c' \quad (7)$$

169 where c' is a constant depending on instrument characteristics and b' is a variable
 170 depending on suspended particle properties (e.g., size, shape, density, elasticity). The log-
 171 linear relation between SNR and SSC is only valid for concentrations less than $1,000\text{mg/L}$
 172 [Salehi and Strom, 2011; Chmiel et al., 2018]; beyond this threshold particle absorption
 173 losses reduce the recorded backscattering signal.

174 The interaction between an acoustic pulse and particles (scattering) is optimal for
 175 coarser individual (unfocculated) particles, with a dependency on the acoustic frequency
 176 such as $kD \approx d$ (or $< d$) where k is the wave number ($2\pi/\lambda$, and λ is the wavelength) and
 177 d the diameter of the particle [Salehi and Strom, 2011]. Hence for a 1MHz acoustic signal,
 178 the optimal backscattering size (diameter) is around $480\mu\text{m}$, while for a 6MHz signal, the
 179 optimal size is around $80\mu\text{m}$. Flocculated particles are characterized by lower backscat-
 180 tering efficiency (1 to 2 order of magnitude lower) [Thorne and Hurther, 2014]. Acoustic
 181 instruments are thus more sensitive to fine to coarse sands than fine flocculated particles
 182 [Salehi and Strom, 2011]: for similar concentrations, the SNR will be stronger for sand
 183 than for fine sediments.

184 **1.4 Combining Optical and Acoustic Measurements: Towards the Sediment Com-** 185 **position Index (SCI)**

186 In coastal and estuarine environments where suspended particles are often charac-
 187 terized by a mixture of fine sediments (including flocs) and sand particles, SSC measure-

188 ments relying on a single technique (optical or acoustic) are ambiguous with respect to
 189 sediment composition. This can lead to misestimates of particle size and concentration
 190 [Thorne *et al.*, 2021], and limits the interpretability and representativeness of the recorded
 191 signal. The objective of the present paper is to combine the use of optical and acoustic
 192 backscatter sensors to estimate the relative fraction of sand in suspension.

193 *Bass et al.* [2007] note that although optical and acoustic backscatter systems are
 194 routinely used together, few studies have taken advantage of using them together to esti-
 195 mate suspended sediment composition in mixed environments. There is a salient differ-
 196 ence in the response of optical and acoustic instruments to changes in suspended particle
 197 size [Ha *et al.*, 2009], which may be exploited to resolve ambiguities.

198 In some cases, it has been assumed that optical or acoustic instruments only observe
 199 a single class of sediment. *Bass et al.* [2002] disregard locally resuspended sand in their
 200 OBS measurements of fine sediment. In studies of tidal channels flanked by intertidal mud
 201 flats, both *Green et al.* [2000] and *van de Kreeke and Hibma* [2005] assumed that optical
 202 sensors detected only silt, while acoustic sensors detected only sand. The interpretation of
 203 a single instrument depends on the assumptions behind its calibration (e.g., an OBS cali-
 204 brated to sandy sediment will overestimate total SSC when fine sediment is also present).
 205 However, instead of ignoring the presence of sand in optical measurements or the pres-
 206 ence of fine sediment in acoustic measurements, paired instruments can more beneficially
 207 be used concurrently and compared [Conner and De Visser, 1992; Green and Boon, 1993;
 208 Hawley, 2004]. In this study, we take advantage of these paired instruments to derive a
 209 Sediment Composition Index (*SCI*) that quantitatively discriminates the presence of sus-
 210 pended sand from mud.

211 This relative optical-acoustic backscatter response can be analyzed by combining
 212 Equations 3 and 7 to obtain:

$$213 \quad SNR = 10 \log_{10}(OBS) + b_{particle} + c_{instr} \quad (8)$$

214 where $b_{particle}$ is a variable parameter function of SPM characteristics and c_{instr} is
 215 a global (optical/acoustic) instrument-related constant. In our study, as instruments were
 216 not calibrated, $b_{particle} + c_{instr}$ are considered as a single constant, the Sediment Com-
 217 position Index (*SCI*). *SCI* is therefore dependent on the characteristics of the sediment
 218 particles being measured and of the instruments being used. Equation 8 can be rearranged

219 to present SCI :

$$220 \quad SCI = 10 \log_{10}(OBS) - SNR \quad (9)$$

221 Considering the high sensitivity of the acoustic sensor to sand and of the optical
222 sensor to fine sediments, SCI is relatively smaller when suspended sand particles dom-
223 inate, and relatively larger when fine sediment dominates suspensions. SCI can thus be
224 used as an indicator of sand or fine sediment dominance.

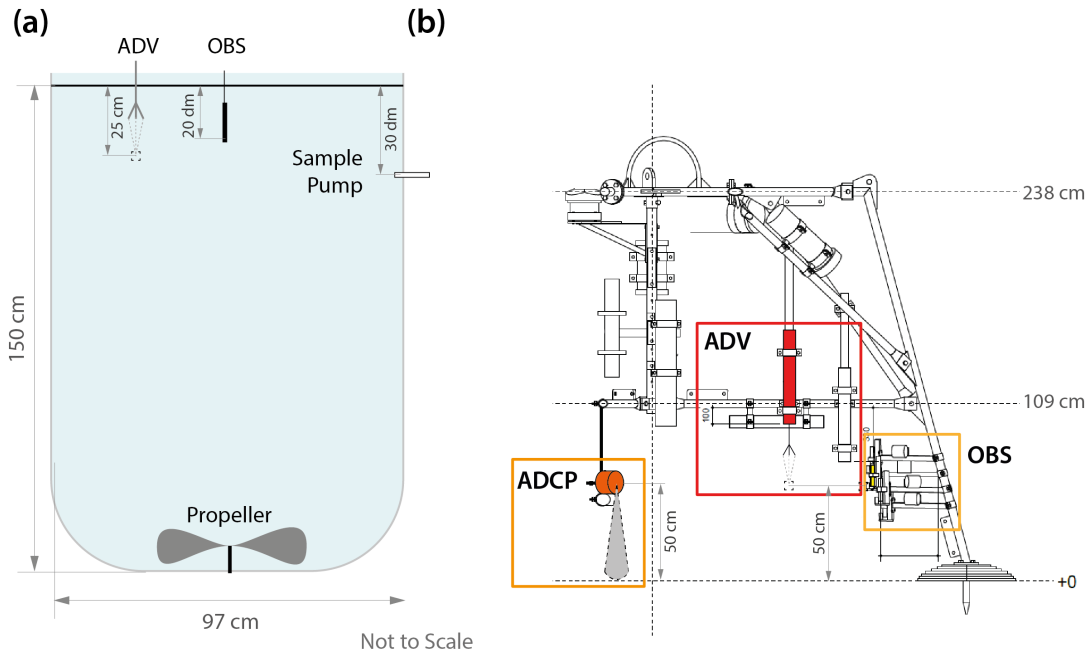
225 **2 Methods**

226 First, we use laboratory measurements as a proof of concept for the SCI , and to
227 quantify the relationship between SCI and the fraction of sand in suspension (f_{sand}).
228 The fraction of mud or fine sediment in suspension can also be directly calculated via
229 $f_{mud} = 100\% - f_{sand}$. We then analyze *in situ* measurements to demonstrate the added
230 value of SCI for investigating the dynamics of mixed-sediment environments. We com-
231 pared optical/acoustic signals measured on Ameland ebb-tidal delta in the Netherlands
232 (Figure 2), calculated SCI and f_{sand} , and put them into context with other simultaneous
233 measurements (tidal stage) and derived parameters (bed shear stress due to waves and cur-
234 rents). By interpreting these measurements, we can test whether SCI is a valid and use-
235 ful indicator of relative suspended sand or fine sediment dominance in estuarine environ-
236 ments.

237 **2.1 Laboratory Experiments**

238 We used the DEXMES (*Dispositif EXpérimental de quantification des Matières En*
239 *Suspension*) tank for our experiments. DEXMES is operated by Ifremer and managed to-
240 gether with Géosciences Océan, Géosciences Rennes, and SHOM (French Hydrographic
241 Service). The glass-walled tank has a volume of approximately $1m^3$ and internal diameter
242 of $0.97m$ (Figure 1), and was filled with fresh water.

250 Two sets of similar experiments were conducted to evaluate SCI at various total sed-
251 iment concentration ranges and sand/fine sediment contents. In Experiment 1, pure ben-
252 tonite ($d_{50} < 63\mu m$) and two classes of well-sorted pure quartz sand ($\rho_s = 2,650kg/m^3$)
253 with median grain sizes $d_{50} \approx 100\mu m$ and $200\mu m$, were used to represent fine and coarse
254 sediment, respectively. The $d_{50} \approx 100\mu m$ sand and $d_{50} \approx 200\mu m$ sands were additionally



243 **Figure 1.** Overview of the DEXMES tank used in the laboratory experiments. (a) Schematic of instrument
 244 setup. During the experiments, the tank contained an Acoustic Doppler Velocimeter (ADV) and Optical
 245 Backscatter Sensor (OBS) mounted just below the surface. An external pump was connected to the tank to ex-
 246 tract suspended sediment samples. (b) Frame used to conduct field measurements (AZG F4), featuring ADV,
 247 OBS, and downward-facing Acoustic Doppler Current Profiler (ADCP) sensors. The ADV and OBS mea-
 248 sured sample volumes 50 cm above the base of the frame, and the ADCP measured a 50 cm profile between
 249 the instrument and the bed.

255 sieved with 100 to 125 μm and 200 to 250 μm meshes, respectively. Conversely, Experi-
256 ment 2 used estuarine mud ($d_{50} < 63\mu\text{m}$) instead of bentonite, and the same sources of
257 sand but without further sieving ($d_{50} = 93\mu\text{m}$ and 210 μm). For simplicity, we hereafter
258 refer to $d_{50} \approx 100\mu\text{m}$ and $d_{50} \approx 200\mu\text{m}$ sand for both experiments.

259 Five sediment composition conditions were investigated for both 100 and 200 μm
260 sand in Experiment 1: pure fine sediment, pure sand, and 3 intermediate mixtures: 25%,
261 50% and 75% sand content (f_{sand}). For each condition, 6 total concentrations were tested
262 stepwise from 15mg/l to 200mg/l. In Experiment 2, fine sediment concentration was held
263 constant at approximately 130mg/l and sand concentration incrementally varied between 0
264 and 1,460mg/l, in order to approximate an estuarine environment with a sandy local bed
265 composition and steady background presence of fine sediment (e.g., *Green et al.* [2000];
266 *van de Kreeke and Hibma* [2005]). Concentrations of both classes of sediment were kept
267 within the linear range of response for each instrument ($< 5,000\text{mg/L}$ of fine sediment
268 and $< 50,000\text{mg/L}$ of sand for the OBS [Downing, 2006] and $< 5,000\text{mg/L}$ for the ADV
269 [Salehi and Strom, 2011]) to avoid ambiguity in the readings. Precise details of the sus-
270 pended sediment concentrations and sand fractions in each experiment are provided in
271 Supporting Information.

272 Vertical concentration gradients were observed within the tank for 200 μm sand,
273 but all instruments and samples measured within 10 cm of the same elevation, leading to
274 comparable sample and sensor data. The propeller at the bottom of the tank was set to a
275 speed of 175rpm to provide high turbulent shear between $G = 30$ and 100s^{-1} , maximizing
276 resuspension and mixture homogeneity while minimizing the formation of bubbles.

277 In Experiments 1 and 2, acoustic backscatter was measured using a Nortek Vec-
278 tor Acoustic Doppler Velocimeter [Nortek AS, 2005], operating at a frequency of 6 MHz,
279 and sampling at 32 Hz (8 Hz in Experiment 2), 25 cm beneath the water surface. Optical
280 backscatter was measured in Experiment 1 using a Wetlabs FLNTU *WET Labs Inc* [2019],
281 sampling at 1 Hz, 20 cm beneath the water surface. In Experiment 2, a Campbell OBS 3+
282 [Campbell Scientific Inc., 2014] was used instead, with similar properties to the Wetlabs
283 FLNTU. To calibrate the optical and acoustic measurements, an external pump was con-
284 nected to the tank 30 cm beneath the surface to extract suspended sediment samples. The
285 instruments were arranged to avoid mutual interference but while sampling a similar ele-
286 vation and hence similar sediment concentrations. All sensors were operated in continuous

287 recording mode for the duration of each experiment, and statistics were computed over a
288 10-11 min period at each sediment concentration level. The median signal-to-noise ratio
289 (SNR) of the three ADV beams and median OBS output were then used to calculate the
290 relative optical-acoustic backscatter index *SCI* from Equation 9.

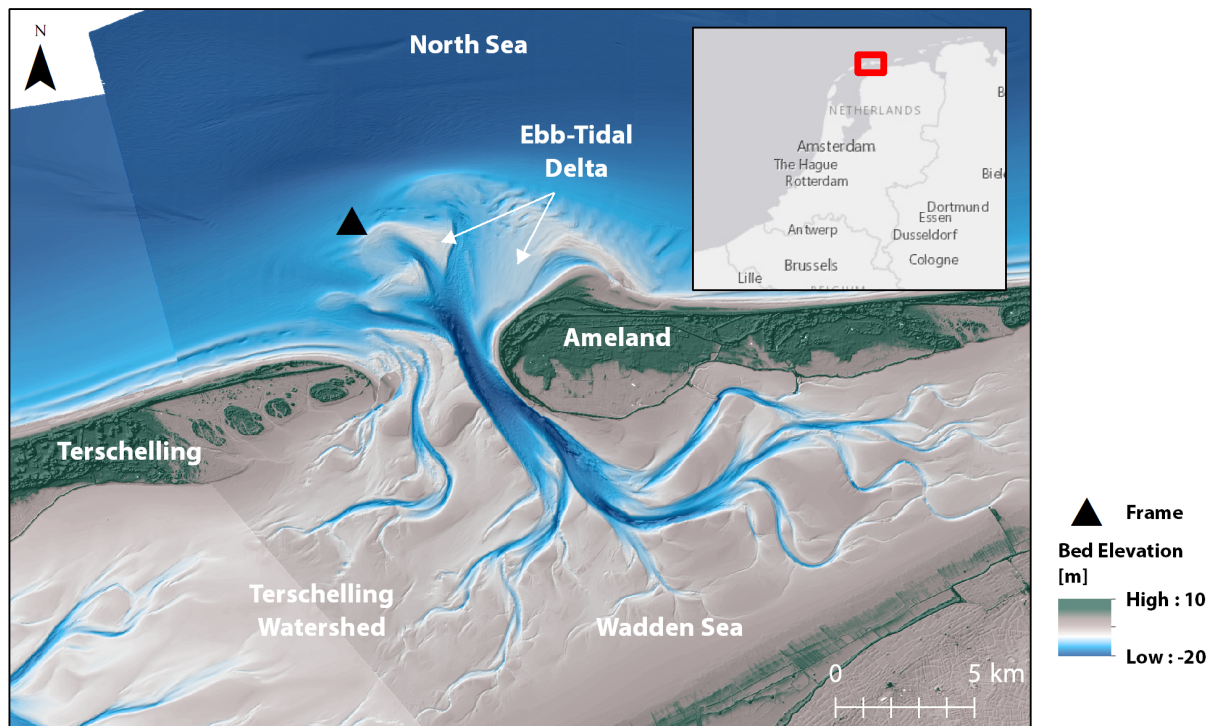
291 **2.2 In Situ Measurements**

292 Ameland Inlet is located in the Netherlands between the sandy barrier islands of
293 Terschelling and Ameland, connecting the North Sea with the Dutch Wadden Sea (Fig-
294 ure 2). The inlet is characterized by a 30 m deep main channel (the “Borndiep”) on its
295 eastern side, and a shifting complex of shoals and channels on its west side. There is a
296 large and highly dynamic ebb-tidal delta complex on the seaward side of the inlet, and a
297 shallow backbarrier basin environment of intertidal shoals and flats on the landward side
298 (the Wadden Sea) [Elias *et al.*, 2019; Lenstra *et al.*, 2019]. The seabed of the ebb-tidal
299 delta of the inlet is mainly well-sorted fine sand (mean $d_{50} = 211\mu\text{m}$, $n = 165$) with
300 mud content generally $< 1\%$, whereas the Wadden Sea has a mud content up to 20% at
301 its landward edge and on the intertidal flats separating Ameland Inlet from adjacent tidal
302 basins [Rijkswaterstaat, 1999; Pearson *et al.*, 2019]. Samples with mud content of $\sim 5\%$
303 can also be found on the North Sea bed beyond the distal end of the ebb-tidal delta.

311 A field measurement campaign was carried out from August 29th to October 9th
312 2017, with the goal of characterizing hydrodynamic and sediment transport processes in
313 the inlet and on its ebb-tidal delta [De Wit *et al.*, 2019; Reniers *et al.*, 2019; Brakenhoff
314 *et al.*, 2019; van der Werf *et al.*, 2019; van Prooijen *et al.*, 2020]. Measurements of flow,
315 waves, suspended particulate matter, bedform dynamics, and water quality were made at
316 4 locations across the site. Measurements considered in this study were obtained at frame
317 AZG-F4 (Figure 2), at the distal end of the ebb-tidal delta, approximately 8m deep.

318 As with the laboratory experiments in Section 2.1, acoustic backscatter was mea-
319 sured using three Nortek Vector Acoustic Doppler Velocimeters (ADV) [Nortek AS, 2005],
320 operating at a frequency of 6 MHz, and sampling at 16 Hz, 20, 50, and 78 cm above the
321 seabed. The median SNR of acoustic backscatter was taken over 30 minute bursts for the
322 deployment period as per Ha *et al.* [2009].

323 Optical backscatter was measured using four Campbell OBS 3+ [Campbell Scien-
324 tific Inc., 2014], sampling at 16 Hz, 20, 30, 50, and 78 cm above the seabed. The OBS



304 **Figure 2.** Overview of measurements during the September 2017 field measurement campaign at Ameland
 305 Inlet, including the frame (AZG-F4) bearing the instruments used in this study. The seabed sediment of the
 306 ebb-tidal delta consists predominantly of very fine sand (with mud content typically < 1%), whereas the
 307 intertidal flats of the Wadden Sea and Terschelling Watershed contain higher mud content [Pearson *et al.*,
 308 2019]. Bathymetry source: Rijkswaterstaat Vaklodgingen. Elevation source: Actueel Hoogtebestand Nederland
 309 (AHN), Rijkswaterstaat. Basemap sources: Esri, HERE, Garmin, OpenStreetMap contributors, and the GIS
 310 user community.

325 was initially calibrated using sandy sediment obtained from the seabed adjacent to the
326 measurement frame. However, *Su et al.* [2016] note that using bed material to calibrate
327 an OBS is “inappropriate” as doing so can introduce errors. On this basis, the calibration
328 was discarded when it was recognized that the additional presence of suspended fine sed-
329 iment in the field rendered it invalid. Thus, the uncalibrated OBS signal is presented here
330 in volts. The median OBS signal over 30 minute bursts was used.

331 Near-bed hydrodynamic conditions during the monitoring period were measured us-
332 ing a high-resolution downward-looking Nortek Aquadopp Acoustic Doppler Current Pro-
333 filer (ADCP-HR) [*Nortek AS*, 2008]. The ADCP sampled at a rate of 4 Hz in 30 minute
334 bursts. These measurements were averaged over the water column between the sensor and
335 the bed (approximately 0.5 m, depending on field conditions) and then median veloci-
336 ties were calculated for each 30 min burst interval. Bed shear stress due to the influence
337 of waves and currents was calculated using the method of *Soulsby* [1997] (with default
338 parameter settings) to give an indication of the potential for local bed material to be re-
339 suspended at the frame. For simplicity, we do not consider the effect of combined wave-
340 current bed shear stresses here, which likely underestimates the frequency of sediment
341 resuspension.

342 To assess the intratidal variation of the field measurements, we classified each 30
343 minute burst into flood tide, high water slack (HWS), ebb tide, and low water slack (LWS)
344 based on an analysis of tidal currents [*Pearson et al.*, 2019]. At the measurement site, the
345 major axis of flow is almost exactly in an east-west direction. Thus, eastward (0 – 179 deg)
346 currents exceeding 0.1m/s were classified as flood, and westward (180 – 359 deg) currents
347 exceeding that threshold as ebb. Velocities below that threshold with positive water sur-
348 face elevations (with respect to MWL) were classified as HWS, and with negative water
349 surface elevations as LWS.

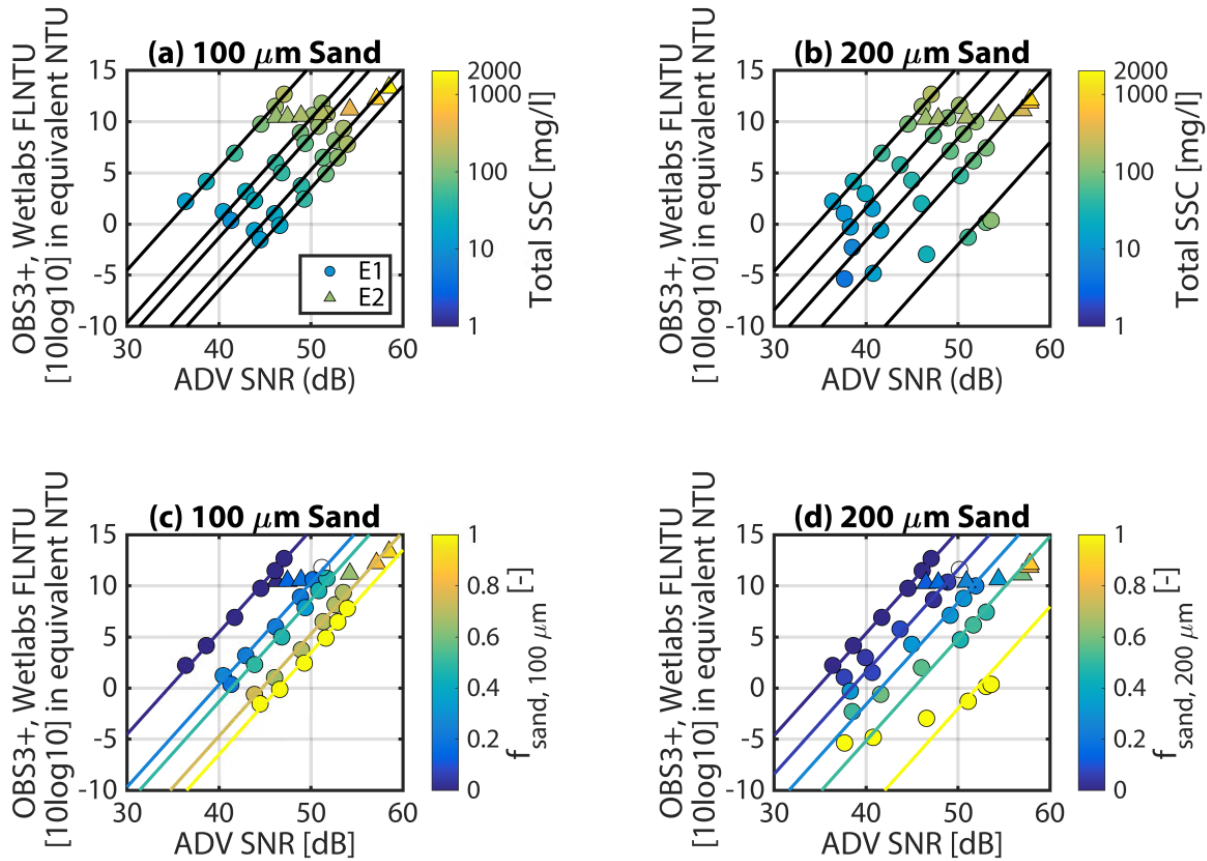
350 **3 Results**

351 **3.1 Laboratory Experiments**

352 **3.1.1 Optical and Acoustic Backscatter**

353 First, we consider the joint response of the optical and acoustic sensors to various
354 sand/fine sediment mixtures: from purely fine suspensions to purely sand suspensions, and
355 with varying total concentrations (Figure 3). Optical turbidity values are recorded in NTU

356 or Volts (Experiment 1 and 2, respectively) depending on the instrument deployed. Read-
 357 ings in Volts are first normalized in equivalent NTU using an offset value in log space
 358 (constant for all Experiment 2 OBS data), so that their values are aligned in Experiments
 359 1 and 2 for purely fine suspension conditions.



360 **Figure 3.** Median acoustic (ADV SNR) and optical backscatter (OBS) as a function of total suspended
 361 sediment concentration (a,b) and suspended sand fraction (f_{sand}) in the laboratory experiments (c,d). (a,c)
 362 Experiments with 100 μm sand. (b,d) Experiments with 200 μm sand. Data from Experiment 1 (E1) mea-
 363 sured with a Wetlabs FLNTU, are marked with circles, while data from Experiment 2 (E2), measured with an
 364 OBS3+, are marked with triangles. Black and coloured lines indicate constant f_{sand} contours.

365 Results from Experiment 1 for 100 μm sand (Figure 3a,c) show that the sensors' re-
 366 sponse is linear in $\log_{10}(OBS)/ADV SNR$ space. This is valid for a range of total sedi-
 367 ment concentration (from 15mg/l to 200mg/l), such that $10\log_{10}(OBS) = SNR + SCI$,
 368 confirming the theoretical relationship (Equation 9). Increasing the sand fraction (f_{sand})
 369 leads to a shift in the data alignment for the different conditions, but lines are still parallel

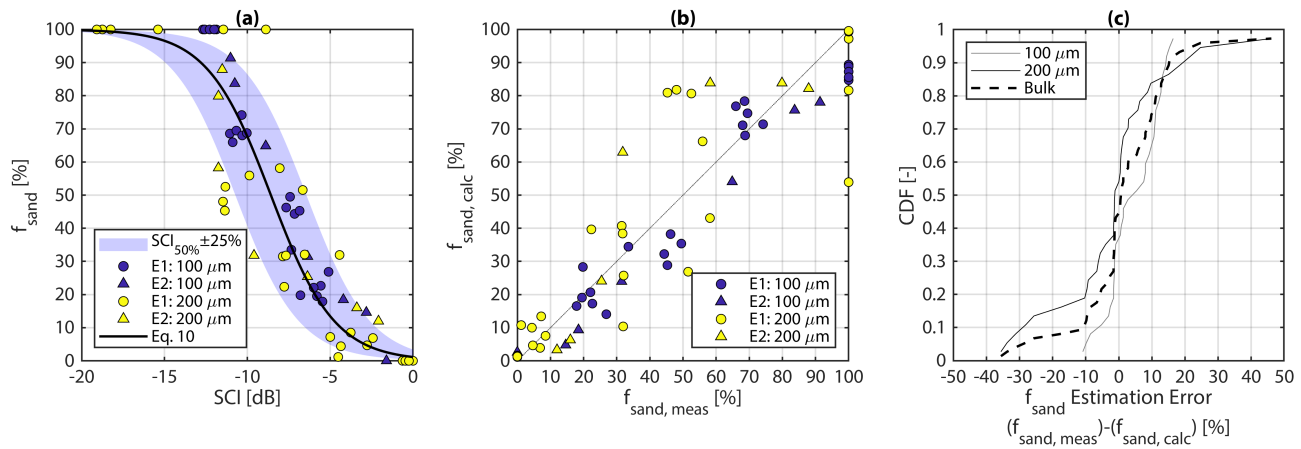
(Figure 3c). That is, for a given $ADVSNR$ value, the optical turbidity value increases as SPM becomes finer. Conversely, for a given optical turbidity value, $ADVSNR$ increases as SPM become sandier. Experiment 2 independently tested a larger total SSC gradient, increasing the sand content from 0 to 100% and total sediment concentration from 135mg/l to 1603mg/l, while progressively adding sand (Figure 3a,c). These results are in full agreement with Experiment 1, with their data points matching the corresponding sand/fine sediment ratio contours as sand content increases.

Similar results are observed for 200 μm sands: $\log_{10}(OBS)/ADV$ pairs are aligned for a given sand content, and these lines are organized parallel to each other (Figure 3b,d). For similar turbidity values, the SNR signal is stronger for 200 μm sand than for 100 μm sand (Figure 3a,b). However, deviations from alignment are observed when sand content dominates (i.e., $f_{sand} > 50\%$) and total concentration is low (i.e., $SSC \leq 50mg/l$). This bias corresponds to the poor sensitivity of the optical sensor to detect low 200 μm particle concentrations, when there are few scatterers in suspension. In such conditions, recorded NTU values range from 0.1 to 0.9 NTU , close to the sensor resolution and lower detection limit. In order to include unbiased data in the analysis, turbidity data below 0.9 NTU are discarded further in the study.

3.1.2 Sediment Composition Index (SCI)

We derived the sediment composition index SCI for the laboratory measurements using Equation 9, and it is shown to be an appropriate proxy for evaluating the sand content (Figure 4a). As a first step towards a generic SCI , we propose to normalize SCI such that $SCI = 0$ in purely fine sediment conditions.

To understand the relationship between the derived SCI and the actual sediment composition, we compare f_{sand} with SCI from both experiments and grain size classes, and find a negative correlation (Figure 4a). A hyperbolic tangent was fit to the data (Equation 10) because f_{sand} should asymptotically reach 0% for maximum SCI (minimum acoustic response, maximum optical response, no sand, only mud), and should tend asymptotically towards 100% for minimum SCI (maximum acoustic response, minimum optical response, only sand, no mud).



392 **Figure 4.** Fraction of sand in total suspended sediment (f_{sand}), calculated from the sediment com-
 393 position index (SCI). (a) f_{sand} as a function of SCI , with Equation 10 fit to both grain sizes in bulk
 394 ($SCI_{50\%} = -8.58$). Blue bands indicate the envelope of uncertainty in f_{sand} , varying $SCI_{50\%}$ by $\pm 25\%$.
 395 Experiments 1 and 2 (E1 and E2, respectively) are indicated, along with the sand grain size used in each
 396 experiment ($R_{100}^2 = 0.957$; $R_{200}^2 = 0.806$; $R_{bulk}^2 = 0.884$). (b) Comparison of experimentally measured
 397 $f_{sand,meas}$ with $f_{sand,calc}$ determined using Equation 10. (c) Cumulative distribution function (CDF) of
 398 sand fraction estimation error ($f_{sand,meas} - f_{sand,calc}$) for each sand grain size class and for all classes
 399 combined in bulk.

$$f_{sand} = \left(\frac{1}{2} + \frac{1}{2} \tanh \left[\frac{(SCI - SCI_{50\%})}{\Delta SCI} \right] \right) \cdot 100\% \quad (10)$$

Where $SCI_{50\%}$ is a constant corresponding to a mixture of 50% sand and 50% mud. It is equal to -8.03 when fitting only 100 μm sand ($R^2_{100\mu m} = 0.954$), -9.63 for 200 μm sand ($R^2_{200\mu m} = 0.848$), and -8.58 when both grain sizes are fit in bulk ($R^2_{bulk} = 0.884$). For the analyses in the rest of this study, we consider $SCI_{50\%} = -8.58$. $\Delta SCI = 3.85$, and indicates the width in variation. Equation 10 allows us to deepen the interpretation of SCI by directly predicting f_{sand} (and by extension, $f_{mud} = 1 - f_{sand}$). It shows good predictive skill when compared with measured f_{sand} for both experiments and grain size classes ($R^2_{100} = 0.957$; $R^2_{200} = 0.806$; $R^2_{bulk} = 0.884$) (Figure 4b). The bulk prediction is accurate for 200 μm sands, as 70% of the calculated sand fractions are associated with an absolute error lower than $\pm 10\%$. Results are the best for the finest sand distribution (100 μm), with more than 85% of the samples estimated with an absolute error below $\pm 10\%$. In case the sand distribution is not known, we also investigated the SCI response to sand content when merging all experimental data (Figure 4c). This bulk index still performs well, with 70% of the calculations with errors within $\pm 10\%$, although the error range is slightly larger, between -30% and $+20\%$.

The clear relationships found in these lab experiments between optical and acoustic backscatter and varying sand content are captured in a single parameter by the SCI . These results confirm that SCI is a relevant proxy for describing the suspended particle composition, and can be used to directly estimate the fraction of sand in suspension (f_{sand}).

3.2 In Situ Measurements

After demonstrating that variations in sediment composition index (SCI) can accurately distinguish relative sand content in controlled laboratory experiments, we evaluated this index using field measurements from Ameland ebb-tidal delta [van Prooijen *et al.*, 2020].

3.2.1 Hydrodynamic Conditions

The measurements from Ameland ebb-tidal delta span 40 days (August 29 to October 8, 2017), or approximately 2.5 spring-neap cycles (Figure 5a). There are two minor

435 storms ($H_s \approx 1m$) on August 30th and September 7th, and two major storms ($H_s > 4m$),
436 *Sebastian* (September 14th, during neap tide) and *Xavier* (October 6th, during spring tide).

457 Spring tide occurs around September 10th, 20th, and October 7th (corresponding
458 to the larger tidal range in Figure 5a). Under calmer conditions, bed shear stresses due to
459 currents ($\tau_{b,c}$) exceed the critical threshold for local sand ($\tau_{cr,211\mu m} = 0.18Pa$) only during
460 spring flood tides (Figure 5c and Figure 6f). These periods with currents strong enough to
461 resuspend or advect sand correspond to flood and ebb stages of the tidal cycle (Figure 5a
462 and Figure 6b).

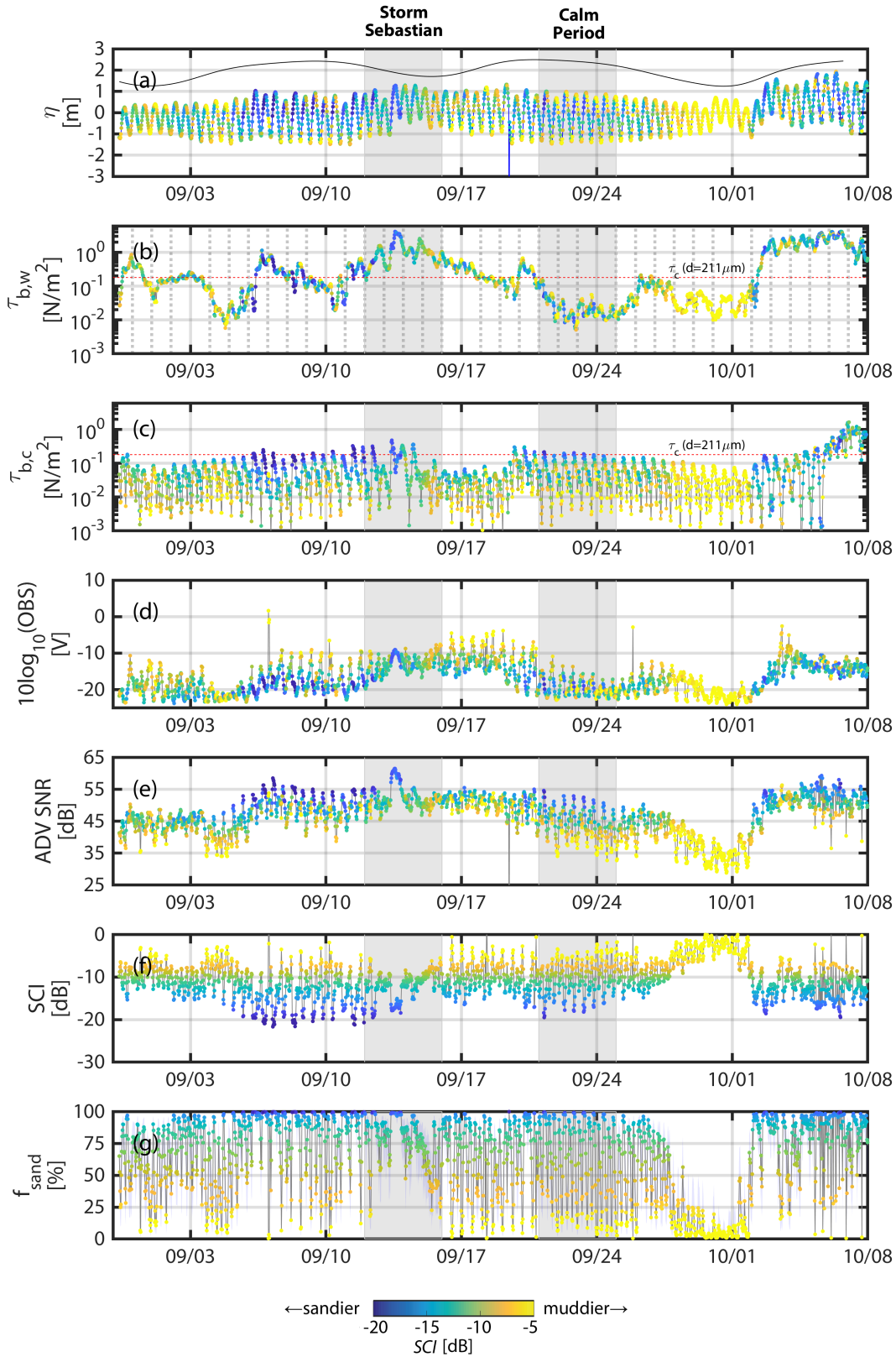
463 Wave-induced bed shear stress $\tau_{b,w}$ is greatest during the storms (Figure 5b and
464 Figure 6c), exceeding $\tau_{cr,211\mu m}$. High bed shear stresses due to currents ($\tau_{b,c}$) are also
465 observed during the two major storms, likely due to wind-induced storm surge and wave-
466 driven currents (Figure 5b). During *Storm Sebastian* on September 14th, eastward currents
467 during the peak of the storm were so strong and persistent that the tide did not reverse (no
468 ebb occurred for nearly 24 hours). During storm periods, $\tau_{b,w}$ is greatest at low tide.

469 **3.2.2 Optical and Acoustic Backscatter**

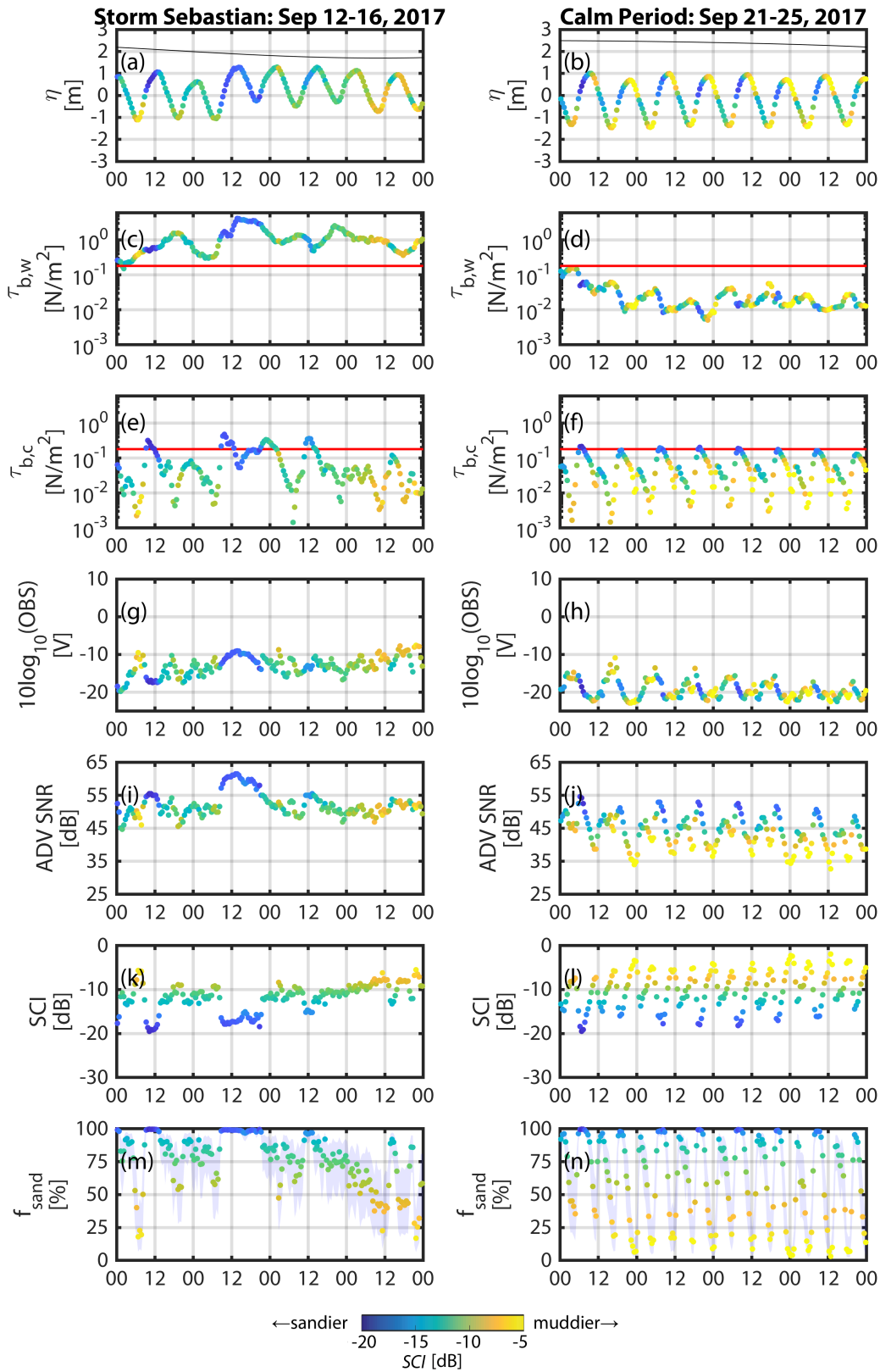
470 Over the total deployment period, OBS measurements show strong tidal variation
471 and a response to individual storm events (Figure 5d and Figure 6h). The largest ADV
472 readings occur during spring tide and the peaks of the two largest storms (Figure 5e and
473 Figure 6i,j), while the lowest ADV SNR readings tend to correspond to calmer periods
474 with low wave stress (Figure 5e and Figure 6j).

475 During Storm Sebastian on September 12th-16th, both SNR and OBS signals strongly
476 increase and tidal variation is weak for the next 2 tidal cycles (Figure 6g,i). Both signals
477 remain relatively high but noisy, and higher background (minimum) readings persist for
478 about a week after the storm.

479 During the calm spring tidal period from September 21st-25th, the influence of
480 waves is minimal and the intratidal dynamics are clear (Figure 6h,j). The OBS signal
481 shows strong M2 (semi-diurnal) tidal oscillations peaking around low water slack. Con-
482 versely, ADV SNR shows mixed M2 and M4 (quarter-diurnal) tidal variation, peaking
483 at flood tide and to a lesser degree at ebb. ADV SNR is lowest at high water slack. The
484 calm period from September 28th to October 2nd coincides with neap tide and exhibits



437 **Figure 5.** Time series of hydrodynamic conditions and backscatter at Ameland ebb-tidal delta Frame
 438 4, with dot colour indicating relative optical-acoustic backscatter index *SCI*. Higher *SCI* (lighter yellow
 439 colours) suggest relatively higher fine sediment content, and lower *SCI* (darker blue colours) suggest rela-
 440 tively higher sand content. (a) Water level relative to the mean depth during the deployment period (8.3m).
 441 The tidal range (indicated with a solid black line) shows spring tide (high values) and neap tide (low values).



447 **Figure 6.** Time series of hydrodynamic conditions and backscatter at Ameland ebb-tidal delta Frame 4,
 448 focusing on Storm Sebastian (Sept 12-16) and a calmer period during spring tide (Sept 21-25). Dot colour indicates
 449 relative optical-acoustic backscatter index *SCI*. Higher *SCI* (lighter yellow colours) suggest relatively
 450 higher fine sediment content, and lower *SCI* (darker blue colours) suggest relatively higher sand content. (a,b)
 451 Water level (η) relative to the mean depth during the deployment period (8.3m). The tidal range (indicated

485 similar dynamics to the pre-storm period at the beginning of the monitoring period, albeit
 486 with lower background OBS and ADV SNR levels and reduced intratidal variability.

487 **3.2.3 Sediment Composition Index (*SCI*) and f_{sand}**

488 From the optical and acoustic backscatter readings, we could then estimate the sus-
 489 pended sediment composition. We calculated *SCI* with Equation 9, using the OBS and
 490 ADV SNR measurements 50 cm above the bed. *SCI* was offset to zero by subtracting
 491 its 99th percentile value. As in the laboratory experiments, this corresponds to a condi-
 492 tion when sand is not likely present. This assumption is corroborated by the calm hy-
 493 drodynamic conditions during moments of high *SCI*. We then applied Equation 10 with
 494 $SCI_{50\%} = -8.58$ (fit to both 100 and 200 μm sand) to the *SCI* time series including the
 495 confidence bands to approximate the fraction of sand in suspension (f_{sand}).

496 At subtidal timescales, *SCI* is lower during storms and spring tides (e.g., Figure 6k,l).
 497 *SCI* reaches its lowest observed values during spring tide, during both calm and stormy
 498 periods (Figure 5b). By contrast, it is highest during calm conditions and neap tide (e.g.,
 499 Figure 5f from Sep 28 to Oct 2). *SCI* is much more dynamic at spring tide, its standard
 500 deviation nearly doubling when compared to neap tide.

501 Over the course of a tidal cycle, *SCI* typically follows a mixed M2 and M4 pattern.
 502 The M4 signal has minima at flood and ebb tide, and is especially pronounced during
 503 spring tidal conditions. Superimposed on this is an M2 variation with its peak centred at
 504 ebb tide. The combination of these two signals results in minimal *SCI* at flood tide when
 505 $\tau_{b,c}$ is high, then a peak at high water slack when $\tau_{b,c}$ is low (Figure 6l). This is followed
 506 by a sharp drop to a secondary minimum at ebb tide (when $\tau_{b,c}$ increases again), and then
 507 a gradual rise to another peak at low water slack. The cycle completes with another rapid
 508 decline in *SCI* at flood tide as currents strengthen. Although *SCI* nearly always peaks at
 509 slack water, the maximum varies between low water slack (e.g., Sep 8-10) and high water
 510 slack (e.g., Sep 21-25).

511 SPM is dominated by sand at ebb and flood tide, when $f_{sand} > 75\%$ (Figure 6n).
 512 Conversely, the suspension consists primarily of fine sediment at high and low water slack
 513 ($f_{sand} < 25\%$). f_{sand} follows an M4 signal, with only weak M2 variations compared to
 514 *SCI*.

515 The presence of waves (indicated by higher wave-induced bed shear stress $\tau_{b,w}$) is
 516 often associated with lower *SCI* (Figure 5b). During Storm Sebastian on September 13th,
 517 *SCI* drops during the peak in the storm, and loses its characteristic M2-M4 tidal variation
 518 for several days (Figure 6k). This corresponds to a period of mainly sand in suspension
 519 ($f_{sand} > 75\%$), with f_{sand} approaching 100% at the peak of the storm (Figure 6m). The
 520 proportion of fine sediment in suspension increases towards the end of the storm, and tidal
 521 variations in f_{sand} begin to return.

522 To further explore the influence of waves on tidal variations in relative optical-acoustic
 523 response, we plot *SCI* as a function of wave ($\tau_{b,w}$) and current-related bed shear stresses
 524 ($\tau_{b,c}$) at each stage of the tidal cycle (Figure 7). We summarize the variability of *SCI* rel-
 525 ative to wave and current forcings (shear stresses), separating results into flood and ebb
 526 tidal phases. In this shear stress space, the dynamics of *SCI* are clearly structured.

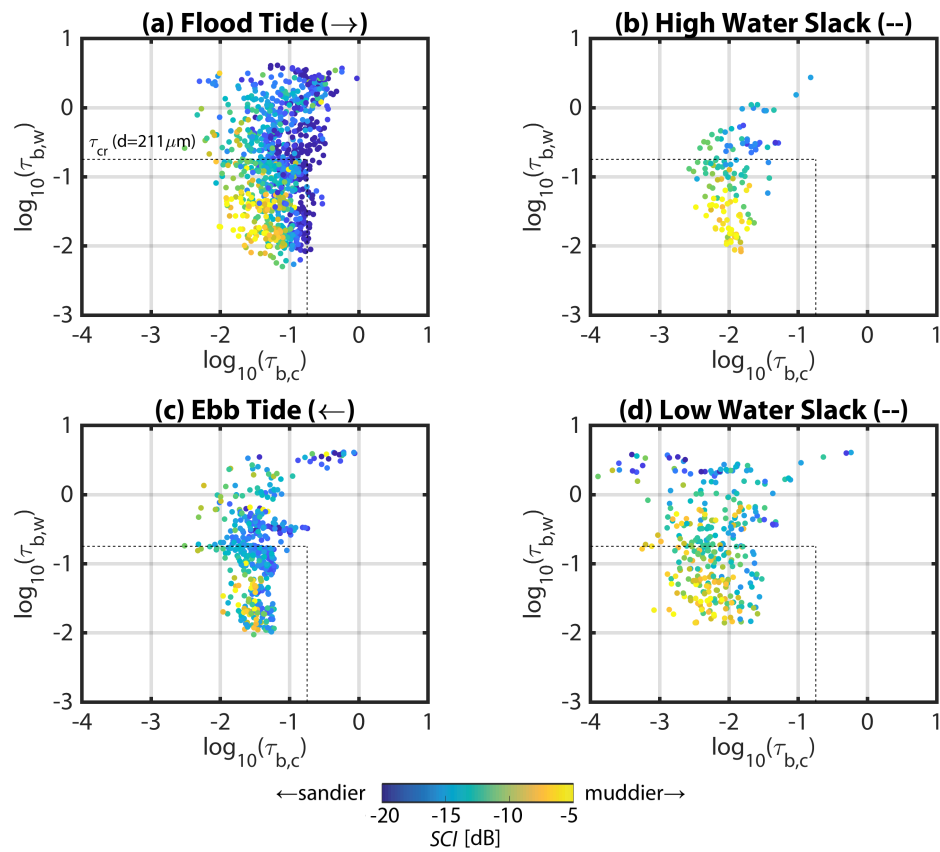
527 During calm flood tides ($\tau_{b,w} < \tau_{cr,211\mu m}$), *SCI* ranges from 0dB during weak cur-
 528 rents to -22dB during stronger currents. A similar pattern is observed during ebb, al-
 529 though generally *SCI* > -15dB. This can be explained by the weaker $\tau_{b,c}$ during maxi-
 530 mum ebb compared with during maximum flood. Both high and low water slack are char-
 531 acterized by relatively high *SCI* (> -10dB). *SCI* reaches < -12dB during slack peri-
 532 ods during wavy conditions. Larger wave-induced stresses are generally associated with
 533 *SCI* < -5dB, although brief peaks in *SCI* can sometimes be observed during storms (Fig-
 534 ure 5).

540 4 Discussion

541 4.1 Interpreting the Dynamics of the Sediment Composition Index (*SCI*)

542 The sediment composition index (*SCI*) is a useful indicator of the relative fractions
 543 of sand and fine sediment in suspension, as validated in laboratory experiments. We fur-
 544 ther demonstrate the application of this index by interpreting the sediment dynamics on
 545 Ameland ebb-tidal delta in light of two main processes: resuspension of local sandy bed
 546 material by waves and strong tides, and tidal advection of fine sediment from locations
 547 outside the ebb-tidal delta. These processes explain the response of optical and acoustic
 548 backscatter measurements, and hence the corresponding dynamics of *SCI*.

549 At subtidal timescales (> 24 hours), the dynamics of *SCI* can be explained in part
 550 by a fortnightly spring-neap cycle. The larger intratidal variation of *SCI* at spring tide is



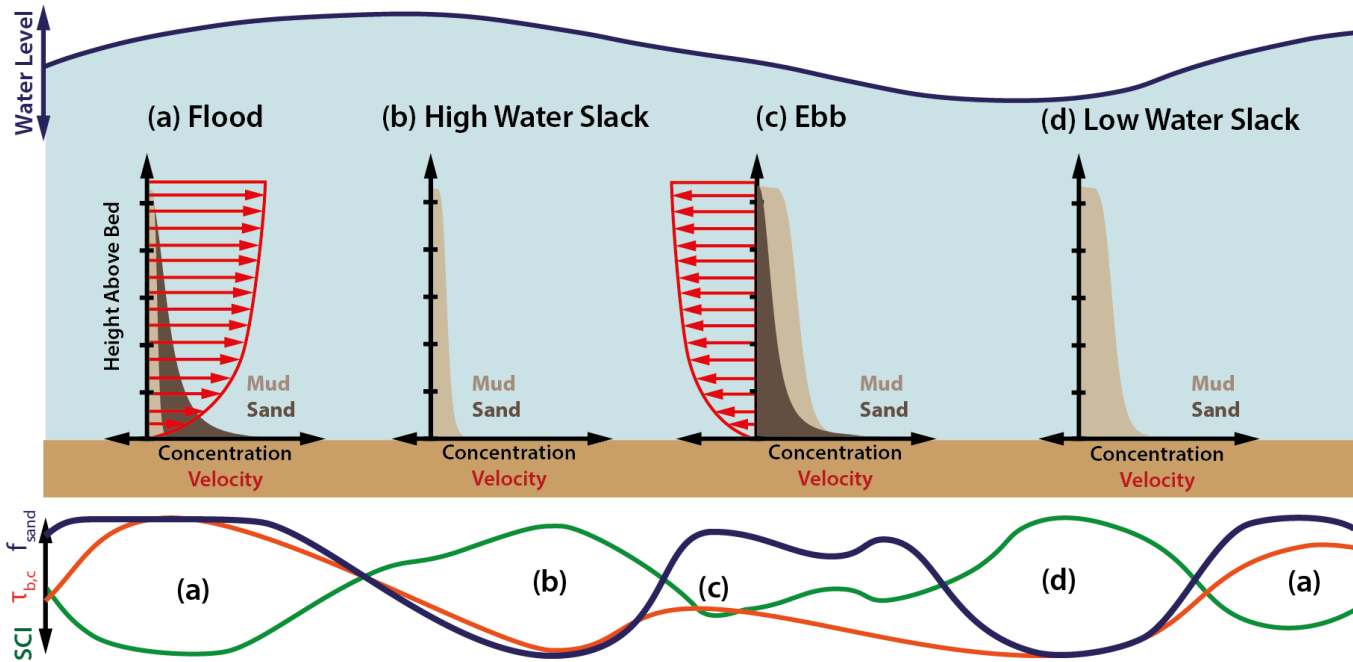
527 **Figure 7.** Sediment composition index SCI (in color) as a function of wave shear stress (vertical axes) and
 528 current shear stress (horizontal axes), at four different stages of the tidal cycle. (a) Flood tide ($u > 0.1m/s$ and
 529 to the east); (b) high water slack ($u < 0.1m/s$ and at high water); (c) ebb tide ($u > 0.1m/s$ and to the west);
 530 (d) low water slack ($u < 0.1m/s$ and at low water). The critical shear stress for local $211\mu m$ sand ($0.18Pa$) is
 531 plotted for reference as a dotted line. Bed shear stresses were computed using *Soulsby* [1997].

551 likely due to the increased resuspension of sand by stronger currents (Figure 5c) and to
552 the greater advection of fine sediment from nearby intertidal flats at late ebb and LWS,
553 similarly to the observations of *Weeks et al.* [1993] and *Fettweis et al.* [1998] at other sites.
554 Conversely, high *SCI* (and thus higher relative proportions of fine sediment in suspension)
555 coincides with the neap tide (e.g., Sep 28-Oct 1) and with lower values of $\tau_{b,w}$ and $\tau_{b,c}$.
556 Without sufficiently strong forcing to resuspend local sand (Figure 5c), only fine sediment
557 can remain in suspension.

558 The observed intratidal variation in *SCI* (Figure 6l) can be explained by the local
559 hydrodynamics and sedimentary environment, and is summarized conceptually in Fig-
560 ure 8. At flood and ebb tide, strong currents are capable of resuspending sand from the
561 local seabed or advecting it from elsewhere nearby, so the corresponding *SCI* values de-
562 crease. Conversely, when sand settles out at slack water, only the suspended fine sediment
563 remains in the water column, explaining the increase in *SCI* value at that time. The result
564 is an M4 signal with minima at flood and ebb tide. This relationship between local resus-
565 pension and local current velocities is also observed by [*Lavelle et al.*, 1984; *Weeks et al.*,
566 1993; *Bass et al.*, 2002; *van de Kreeke and Hibma*, 2005].

577 Modulating the M4 *SCI* signal is an M2 signal with its maximum centred at ebb
578 tide. This M2 signal can be explained by the semidiurnal migration of a strong landward
579 fine sediment concentration gradient in the channels of Ameland basin [*Postma*, 1961].
580 Remote sensing indicates that this turbid water mass can be ejected several kilometres
581 seaward of the inlet and across the ebb-tidal delta at ebb [*Pearson et al.*, 2019], which
582 causes the corresponding *SCI* to increase. This muddy water mass is then displaced by
583 less turbid oceanic water on the flood tide, so *SCI* decreases again. This semidiurnal
584 transport pattern is widely observed at other sites where there is a persistent gradient in
585 suspended fine sediment concentration [*Weeks et al.*, 1993; *Green et al.*, 2000; *Bass et al.*,
586 2002; *van de Kreeke and Hibma*, 2005].

587 To fully explain the *SCI* dynamics at Ameland, the episodic influence of storms
588 must also be accounted for. If waves are sufficiently large ($\tau_{b,w} > \tau_{cr,211\mu m}$), then the ma-
589 jority of local sand can be mobilized, which can result in low values of *SCI* regardless of
590 the tidal stage. Conversely, the periods with the lowest *SCI* (suggesting lower proportions
591 of sand in suspension and relatively more fine sediment) coincide mainly with periods of
592 low wave action (e.g., Sep 28-Oct 1).



567 **Figure 8.** Conceptual model of tidally-driven mixed sand-fine sediment transport at the study site on Ame-
 568 land ebb-tidal delta. A normalized example time series of sediment composition index (*SCI*), bed shear stress
 569 due to currents ($\tau_{b,c}$), and fraction of sand in suspension (f_{sand}) over a tidal cycle are indicated below. (a)
 570 At flood tide, strong currents locally resuspend sand, but carry few fine particles from the North Sea, so *SCI*
 571 is low. (b) At high water slack, currents are too weak to mobilize sand, so total concentrations are relatively
 572 low and consist only of fines, so *SCI* is higher. (c) At ebb tide, strong currents locally resuspend sand, though
 573 less than at flood tide, so *SCI* decreases again. These ebb currents also carry with them fine particles from
 574 the muddy and biologically productive Wadden Sea. (d) At low water slack, currents are too weak to mobilize
 575 sand, leaving only the fine material advected from the Wadden Sea at ebb, which begins to settle, resulting in
 576 higher *SCI*.

593 During periods with large waves, *SCI* may be influenced not just by an increased
594 capacity for local resuspension of sand, but also by wind and wave-induced fine sediment
595 resuspension. This is reflected in the *SCI* signal during Storm Sebastian (Figure 6). Even
596 when bed shear stresses due to waves and currents greatly exceed $\tau_{cr,211\mu m}$, *SCI* seldom
597 drops below $-15dB$ and f_{sand} remains between 50 – 90% for most of the storm. In the
598 latter half of the storm, f_{sand} decreases as sand settles out, while fine sediment remains
599 in suspension. This fine material can originate from two locations: the Wadden Sea tidal
600 basin or the bed of the North Sea. During storms, tidal flats in Ameland basin may easily
601 lose the surface layers of sediment deposited in calm periods [Postma, 1961]. In a similar
602 case study, Green *et al.* [2000] found that wave activity on nearby intertidal flats was the
603 principal determinant of suspended fine sediment load advected through a tidal channel.
604 However, storms may also remobilize fine sediment which accumulates in the bed of the
605 North Sea [van der Hout *et al.*, 2017; Flores *et al.*, 2017; Hendriks *et al.*, 2020]. Instanta-
606 neous bed shear stress does not tell the whole story of suspended sediment composition: it
607 is also necessary to account for spatial and temporal variations in the supply of fine sedi-
608 ment.

609 Our interpretation of *SCI* based on theoretical considerations and the laboratory re-
610 sults are fully supported by the local hydrodynamics and sedimentological context. *SCI*
611 thus provides a novel and valuable characterization of the suspended sediment dynamics
612 on Ameland ebb-tidal delta. This metric is especially useful for mixed-sediment environ-
613 ments like Ameland where optical and acoustic measurements are otherwise ambiguous
614 when viewed in isolation.

615 4.2 Limitations & Outlook

616 Having been conceptually validated by laboratory and field measurements, there are
617 many opportunities for further developing the *SCI* and improving its applicability. The
618 next steps towards a more quantitative evaluation of sediment composition lie in the accu-
619 mulation of larger datasets and in quantifying the component of *SCI* specific to the instru-
620 ments being used (the c_{instr} term of Equation 8, which is invariant with SPM).

621 For a more generic *SCI*, we propose a reference calibration of optical and acous-
622 tic sensors to evaluate the instrument constant c_{instr} (Equation 8), using NTU/BTU (for-
623 mazin calibration) for optical systems, and monodispersed glass beads for acoustic par-

624 ticles, similarly to the calibration procedure for an ABS system (e.g., *Thorne and Meral*
625 [2008]). With calibrated scatterers, the sonar equation (Equation 4) can be fully evaluated,
626 the instrument constant c_{instr} is the only unknown. Acoustic backscatter is sensitive to the
627 acoustic frequency of the transducers: the *SCI* dynamics will be different from 1 MHz to
628 6 MHz sensors, because each sensor will respond differently to sediment of a given grain
629 size and concentration. Similarly, optical sensors will provide different NTU values de-
630 pending on whether the optical sensor is based on backscatter (e.g., OBS 3+ [*Campbell*
631 *Scientific Inc.*, 2014], Seapoint *Seapoint Sensors Incorporated* [2013], or Wetlabs [*WET-*
632 *Labs*, 2010]) or sidescattering (e.g., YSI 6600 [*YSI Incorporated*, 2012]). Many additional
633 laboratory experiments would be required in order to determine c_{instr} and make a full
634 set of conversion factors for each type of instrument. By applying these calibrations, *SCI*
635 could become generic, at least for similar instruments. However, even without quantifying
636 c_{instr} directly, *SCI* provides useful information on suspended sediment composition when
637 its dynamics are considered in the context of local hydrodynamic and sedimentological
638 conditions.

639 Additional laboratory experiments must be carried out with a wider variety of sedi-
640 ment mixtures and concentrations. We expect that most of the variability of *SCI* is caused
641 to first order by the presence of sand in suspension, because sand has a relatively stronger
642 influence on acoustic backscatter than flocs of comparable size [*Thorne and Hurther*, 2014].
643 However, the influence of flocculation on the variability of *SCI* requires further investiga-
644 tion.

645 Field measurements should also be collected from sites with different sedimentary
646 characteristics under a range of hydrodynamic conditions in order to generalize the conclu-
647 sions of the present study and *SCI*– f_{sand} relationships like Equation 10. Samples pumped
648 at regular intervals (e.g., *Beamsley et al.* [2001]) or better yet, at moments triggered by
649 specific turbidity levels, would provide a more representative basis for calibrating opti-
650 cal and acoustic measurements. Fortunately, analyzing *SCI* dynamics of additional field
651 sites is already possible, since optical and acoustic instruments are frequently paired to-
652 gether in the field (e.g., *Fugate and Friedrichs* [2002]; *Voulgaris and Meyers* [2004]; *Moura*
653 *et al.* [2011]; *Flores et al.* [2018]; *Zhu et al.* [2019]; *Lin et al.* [2020]; *de Vet et al.* [2020];
654 *Colosimo et al.* [2020]; *Pomeroy et al.* [2021]). Our approach thus gives added value to
655 existing datasets by providing an additional, simple-to-calculate metric for interpreting
656 sediment dynamics.

657 These additional efforts to make *SCI* more general and to better understand the un-
658 derlying physics will strengthen the usefulness and applicability of the metric. This will
659 lead to new insights into the dynamics of mixed sediment environments where ambiguity
660 due to suspended sediment composition previously limited the information that could be
661 obtained from optical and acoustic measurements.

662 **5 Conclusions**

663 The sediment composition index (*SCI*) derived in this study quantifies the suspended
664 sediment composition in mixed-sediment environments. It does so using the relative inten-
665 sity of optical and acoustic backscatter signals, as these two measurement techniques have
666 different sensitivities to sand and fine sediment (Equation 9). *SCI* can be used to estimate
667 the fraction of sand and fine sediment in suspension (f_{sand} and f_{mud}) in marine environ-
668 ments. Here, we verify the theoretical response of these optical and acoustic instruments
669 in laboratory experiments. *SCI* is negatively correlated with the fraction of sand in sus-
670 pension (Equation 10).

671 We successfully applied this approach to *in situ* measurements on the ebb-tidal delta
672 of Ameland Inlet in the Netherlands. *SCI* shows a clear M4 variation associated with sus-
673 pension of local sand, modulated by an M2 variation associated with suspended fine sed-
674 iment advected from the nearby Wadden Sea. Lower values of *SCI* (indicating a stronger
675 acoustic response) and higher f_{sand} are observed under more energetic conditions when
676 sand is expected to dominate the suspension (e.g., spring flood tide or strong wave con-
677 ditions). Conversely, *SCI* increases (indicating a stronger optical response) and f_{sand}
678 reduces in calmer conditions and at slack water, when the suspended sediment consists
679 mainly of fine sediment.

680 This approach reduces the ambiguity of suspended sediment composition in mixed
681 sediment environments. Furthermore, it adds value to existing sets of measurements since
682 simultaneous optical/acoustic measurements have frequently been carried out together in
683 sediment transport studies. Being able to discern between different types of sediment in
684 suspension will increase confidence in the interpretation of suspended sediment concentra-
685 tion measurements. This can ultimately improve estimates of sediment fluxes, leading to
686 deeper understanding of coastal systems and enable better-informed coastal management
687 decision-making.

688 **Acknowledgments**

689 This work is part of the research programme ‘‘Collaboration Program Water’’ with
 690 project number 14489 (SEAWAD), which is (partly) financed by NWO Domain Applied
 691 and Engineering Sciences. SGP was partly funded by ISblue within their Foreign Student
 692 Mobility Programme. Special thanks to the Dutch Ministry of Infrastructure and Water
 693 Management (Rijkswaterstaat and Rijksrederij) for their ongoing support as part of the
 694 Kustgenese2.0 project. Data archiving for this study is currently underway, with some data
 695 already publicly available at 4TU Centre for Research Data at <https://doi.org/10.4121/collection:seawad>
 696 *Delft University of Technology et al.* [2019]. Details of this dataset can be found in *van*
 697 *Prooijen et al.* [2020] and *van der Werf et al.* [2019]. Additional data files have been tem-
 698 porarily included here as supporting information for the review process:

699 <https://surfdrive.surf.nl/files/index.php/s/q1slh1EqhRkUh11>

700 **References**

701 Bass, S. J., J. N. Aldridge, I. N. McCave, and C. E. Vincent (2002), Phase relationships
 702 between fine sediment suspensions and tidal currents in coastal seas, *Journal of Geo-*
 703 *physical Research: Oceans*, 107(10), 1–14, doi:10.1029/2001jc001269.

704 Bass, S. J., I. N. McCave, J. M. Rees, and C. E. Vincent (2007), Sand and mud flux es-
 705 timates using acoustic and optical backscatter sensors: Measurements seaward of the
 706 Wash, southern North Sea, *Geological Society Special Publication*, 274, 25–35, doi:
 707 10.1144/GSL.SP.2007.274.01.04.

708 Beamsley, B. J., K. P. Black, and T. Healy (2001), Micro-scale Pumped Measurements of
 709 Suspended Sediment Over a Mixed Sand/Mud Bed: Profiles, Grain Sizes and Sediment
 710 Diffusivity, *Journal of Coastal Research*, (34), 342–356.

711 Brakenhoff, L., M. Kleinans, G. Ruessink, and M. Vegt (2019), Spatio-temporal char-
 712 acteristics of small-scale wave-current ripples on the Ameland ebb-tidal delta, *Earth*
 713 *Surface Processes and Landforms*, doi:10.1002/esp.4802.

714 Campbell Scientific Inc. (2014), OBS-3+ and OBS300 Suspended Solids and Turbidity
 715 Monitors, *Tech. rep.*, Campbell Scientific Inc., Logan, Utah.

716 Chapalain, M., R. Verney, M. Fettweis, M. Jacquet, D. Le Berre, and P. Le Hir (2019),
 717 Investigating suspended particulate matter in coastal waters using the fractal theory,
 718 *Ocean Dynamics*, 69(1), 59–81, doi:10.1007/s10236-018-1229-6.

- 719 Chmiel, O., I. Baselt, and A. Malcherek (2018), Applicability of Acoustic Concentration
720 Measurements in Suspensions of Artificial and Natural Sediments Using an Acoustic
721 Doppler Velocimeter, *Acoustics*, 1(1), 59–77, doi:10.3390/acoustics1010006.
- 722 Colosimo, I., P. L. de Vet, D. S. van Maren, A. J. Reniers, J. C. Winterwerp, and
723 B. C. van Prooijen (2020), The impact of wind on flow and sediment transport
724 over intertidal flats, *Journal of Marine Science and Engineering*, 8(11), 1–26, doi:
725 10.3390/jmse8110910.
- 726 Conner, C. S., and A. M. De Visser (1992), A laboratory investigation of particle size
727 effects on an optical backscatterance sensor, *Marine Geology*, 108(2), 151–159, doi:
728 10.1016/0025-3227(92)90169-I.
- 729 de Vet, P. L., B. C. van Prooijen, I. Colosimo, N. Steiner, T. Ysebaert, P. M. Herman, and
730 Z. B. Wang (2020), Variations in storm-induced bed level dynamics across intertidal
731 flats, *Scientific Reports*, 10(1), 1–15, doi:10.1038/s41598-020-69444-7.
- 732 De Wit, F., M. Tissier, and A. J. Reniers (2019), Characterizing wave shape evolution
733 on an ebb-tidal shoal, *Journal of Marine Science and Engineering*, 7(10), 1–20, doi:
734 10.3390/jmse7100367.
- 735 Delft University of Technology, Utrecht University, and University of Twente (2019), *SEA-*
736 *WAD: SEdiment supply At the WAdden Sea ebb-tidal Delta*, 4TU.Centre for Research
737 Data, doi:10.4121/collection:seawad.
- 738 Downing, J. (2006), Twenty-five years with OBS sensors: The good, the bad, and the
739 ugly, *Continental Shelf Research*, 26(17-18), 2299–2318, doi:10.1016/j.csr.2006.07.018.
- 740 Elias, E. P., A. J. F. Van Der Spek, S. G. Pearson, and J. Cleveringa (2019), Under-
741 standing sediment bypassing processes through analysis of high- frequency observa-
742 tions of Ameland Inlet , the Netherlands, *Marine Geology*, 415(May), 105,956, doi:
743 10.1016/j.margeo.2019.06.001.
- 744 Fettweis, M., M. Sas, and J. Monbaliu (1998), Seasonal, neap-spring and tidal variation of
745 cohesive sediment concentration in the Scheldt Estuary, Belgium, *Estuarine, Coastal and*
746 *Shelf Science*, 47(1), 21–36, doi:10.1006/ecss.1998.0338.
- 747 Fettweis, M., R. Riethmüller, R. Verney, M. Becker, J. Backers, M. Baeye, M. Chapalain,
748 S. Claeys, J. Claus, T. Cox, J. Deloffre, D. Depreiter, F. Druine, G. Flöser, S. Grünler,
749 F. Jourdin, R. Lafite, J. Nauw, B. Nechad, R. Röttgers, A. Sottolichio, T. V. Engeland,
750 W. Vanhaverbeke, H. Vereecken, T. Van Engeland, W. Vanhaverbeke, and H. Vereecken
751 (2019), Uncertainties associated with in situ high-frequency long-term observations of

- 752 suspended particulate matter concentration using optical and acoustic sensors, *Progress*
 753 *in Oceanography*, 178(July 2018), 102,162, doi:10.1016/j.pocean.2019.102162.
- 754 Flemming, B. W., and K. Ziegler (1995), High-Resolution Grain Size Distribution Patterns
 755 and Textural Trends in the Backbarrier Environment of Spiekeroog Island (Southern
 756 North Sea), *Senckenbergiana Maritima*, 26, 1–24.
- 757 Flores, R. P., S. Rijnsburger, A. R. Horner-Devine, A. J. Souza, and J. D. Pietrzak (2017),
 758 The impact of storms and stratification on sediment transport in the Rhine region of
 759 freshwater influence, *Journal of Geophysical Research: Oceans*, 122(5), 4456–4477, doi:
 760 10.1002/2016JC012362.
- 761 Flores, R. P., S. Rijnsburger, S. Meirelles, A. R. Horner-Devine, A. J. Souza, J. D.
 762 Pietrzak, M. Henriquez, and A. J. Reniers (2018), Wave generation of gravity-driven
 763 sediment flows on a predominantly sandy seabed, *Geophysical Research Letters*, 45(15),
 764 7634–7645, doi:10.1029/2018GL077936.
- 765 Fugate, D. C., and C. T. Friedrichs (2002), Determining concentration and fall velocity
 766 of estuarine particle populations using adv, obs and lisst, *Continental Shelf Research*,
 767 22(11-13), 1867–1886, doi:10.1016/S0278-4343(02)00043-2.
- 768 Green, M. O., and J. D. Boon (1993), The measurement of constituent concentrations in
 769 nonhomogeneous sediment suspensions using optical backscatter sensors, *Marine Geol-*
 770 *ogy*, 110(1-2), 73–81, doi:10.1016/0025-3227(93)90106-6.
- 771 Green, M. O., R. G. Bell, T. J. Dolphin, and A. Swales (2000), Silt and sand transport
 772 in a deep tidal channel of a large estuary (Manukau Harbour, New Zealand), *Marine*
 773 *Geology*, 163(1-4), 217–240, doi:10.1016/S0025-3227(99)00102-4.
- 774 Ha, H. K., W. Y. Hsu, J. P. Maa, Y. Y. Shao, and C. W. Holland (2009), Using ADV
 775 backscatter strength for measuring suspended cohesive sediment concentration, *Conti-*
 776 *ental Shelf Research*, 29(10), 1310–1316, doi:10.1016/j.csr.2009.03.001.
- 777 Hawley, N. (2004), A comparison of suspended sediment concentrations measured by
 778 acoustic and optical sensors, *Journal of Great Lakes Research*, 30(2), 301–309, doi:
 779 10.1016/S0380-1330(04)70348-2.
- 780 Hendriks, H. C., B. C. van Prooijen, S. G. Aarninkhof, and J. C. Winterwerp (2020), How
 781 human activities affect the fine sediment distribution in the Dutch Coastal Zone seabed,
 782 *Geomorphology*, 367, 107,314, doi:10.1016/j.geomorph.2020.107314.
- 783 Hoitink, A. J., and P. Hoekstra (2005), Observations of suspended sediment from ADCP
 784 and OBS measurements in a mud-dominated environment, *Coastal Engineering*, 52(2),

- 785 103–118, doi:10.1016/j.coastaleng.2004.09.005.
- 786 Lavelle, J. W., H. O. Mofjeld, and E. T. Baker (1984), An in situ erosion rate for a fine-
787 grained marine sediment., doi:10.1029/JC089iC04p06543.
- 788 Lenstra, K. J., S. R. Pluis, W. Ridderinkhof, G. Ruessink, and M. van der Vegt (2019),
789 Cyclic channel-shoal dynamics at the Ameland inlet: the impact on waves, tides, and
790 sediment transport, *Ocean Dynamics*, 69(4), 409–425, doi:10.1007/s10236-019-01249-3.
- 791 Lin, J., Q. He, L. Guo, B. C. van Prooijen, and Z. B. Wang (2020), An integrated op-
792 tic and acoustic (IOA) approach for measuring suspended sediment concentration
793 in highly turbid environments, *Marine Geology*, 421(October 2019), 106,062, doi:
794 10.1016/j.margeo.2019.106062.
- 795 Many, G., X. Durrieu de Madron, R. Verney, F. Bourrin, P. R. Renosh, F. Jourdin, and
796 A. Gangloff (2019), Geometry, fractal dimension and settling velocity of flocs dur-
797 ing flooding conditions in the Rhône ROFI, *Estuarine, Coastal and Shelf Science*,
798 219(January), 1–13, doi:10.1016/j.ecss.2019.01.017.
- 799 Moura, M. G., V. S. Quaresma, A. C. Bastos, and P. Veronez (2011), Field observa-
800 tions of SPM using ADV, ADP, and OBS in a shallow estuarine system with low
801 SPM concentration-Vitória Bay, SE Brazil, *Ocean Dynamics*, 61(2-3), 273–283, doi:
802 10.1007/s10236-010-0364-5.
- 803 Nortek AS (2005), Vector Current Meter - User Manual, *Tech. Rep. N 300-100 Rev. H*,
804 Nortek Group, Vangkroken, Norway.
- 805 Nortek AS (2008), Aquadopp High Resolution - User Manual, *Tech. Rep. AHR00-0101-*
806 *0508*, Nortek AS, Vangkroken, Norway.
- 807 Öztürk, M. (2017), Sediment size effects in acoustic doppler velocimeter-derived estimates
808 of suspended sediment concentration, *Water (Switzerland)*, 9(7), doi:10.3390/w9070529.
- 809 Pearson, S. G., B. van Prooijen, F. de Wit, H. Meijer-Holzauer, A. de Loeff,
810 and Z. B. Wang (2019), Observations of Suspended Particle Size Distribution
811 on an Energetic Ebb-Tidal Delta, *Coastal Sediments 2019*, pp. 1991–2003, doi:
812 10.1142/9789811204487_0172.
- 813 Pomázi, F., and S. Baranya (2020), Comparative assessment of fluvial suspended sediment
814 concentration analysis methods, *Water*, 12(3), doi:10.3390/w12030873.
- 815 Pomeroy, A. W., C. D. Storlazzi, K. J. Rosenberger, R. J. Lowe, J. E. Hansen, and M. L.
816 Buckley (2021), The contribution of currents, sea?swell waves, and infragravity waves
817 to suspended?sediment transport across a coral reef?lagoon system., *Journal of Geo-*

- 818 *physical Research: Oceans*, pp. 1–26, doi:10.1029/2020jc017010.
- 819 Postma, H. (1961), Suspended Matter and Secchi Disc Visibility in Coastal Waters,
820 *Netherlands Journal of Sea Research*, 1(3), 359–390.
- 821 Reniers, A. J., F. P. de Wit, M. F. S. Tissier, S. G. Pearson, L. B. Brakenhoff, M. van der
822 Vegt, J. Mol, and B. C. van Prooijen (2019), Wave-Skewness and Current-Related Ebb-
823 Tidal Sediment Transport: Observations and Modeling, in *Coastal Sediments 2019*, pp.
824 2018–2028, St. Petersburg, Florida, doi:10.1142/9789811204487_0174.
- 825 Rijkswaterstaat (1999), *Sedimentatlas Waddenzee*, 36–38 pp., Rijkswaterstaat, Haren,
826 Netherlands.
- 827 Salehi, M., and K. Strom (2011), Using velocimeter signal to noise ratio as a surrogate
828 measure of suspended mud concentration, *Continental Shelf Research*, 31(9), 1020–
829 1032, doi:10.1016/j.csr.2011.03.008.
- 830 Seapoint Sensors Incorporated (2013), Seapoint turbidity meter user manual, *Tech. rep.*,
831 Seapoint Sensors, Inc, Exeter, NH.
- 832 Son, C. S., B. W. Flemming, and A. Bartholomä (2011), Evidence for sediment recircula-
833 tion on an ebb-tidal delta of the East Frisian barrier-island system, southern North Sea,
834 *Geo-Marine Letters*, 31(2), 87–100, doi:10.1007/s00367-010-0217-8.
- 835 Soulsby, R. L. (1997), *Dynamics of marine sands: a manual for practical applications*,
836 Thomas Telford.
- 837 Su, M., P. Yao, Z. B. Wang, C. Zhang, Y. Chen, and M. J. Stive (2016), Conversion of
838 electro-optical signals to sediment concentration in a silt-Åsand suspension environ-
839 ment, *Coastal Engineering*, 114, 284–294, doi:10.1016/j.coastaleng.2016.04.014.
- 840 Sutherland, T. F., P. M. Lane, C. L. Amos, and J. Downing (2000), The calibration of op-
841 tical backscatter sensors for suspended sediment of varying darkness levels, *Marine Ge-*
842 *ology*, 162(2-4), 587–597, doi:10.1016/S0025-3227(99)00080-8.
- 843 Thorne, P. D., and D. M. Hanes (2002), A review of acoustic measurement of small-scale
844 sediment processes, *Continental Shelf Research*, 22(4), 603–632, doi:10.1016/S0278-
845 4343(01)00101-7.
- 846 Thorne, P. D., and D. Hurther (2014), An overview on the use of backscattered sound
847 for measuring suspended particle size and concentration profiles in non-cohesive
848 inorganic sediment transport studies, *Continental Shelf Research*, 34, 97–118, doi:
849 10.1016/j.csr.2013.10.017.

- 850 Thorne, P. D., and R. Meral (2008), Formulations for the scattering properties of sus-
 851 pended sandy sediments for use in the application of acoustics to sediment transport
 852 processes, *Continental Shelf Research*, 28(2), 309–317, doi:10.1016/j.csr.2007.08.002.
- 853 Thorne, P. D., P. J. Hardcastle, and R. L. Soulsby (1993), Analysis of Acoustic Measure-
 854 ments of Suspended Sediments, *Journal of Geophysical Research*, 98(92), 899–910.
- 855 Thorne, P. D., I. D. Lichtman, and D. Hurther (2021), Acoustic scattering charac-
 856 teristics and inversions for suspended concentration and particle size above mixed
 857 sand and mud beds, *Continental Shelf Research*, 214(November 2020), 104,320, doi:
 858 10.1016/j.csr.2020.104320.
- 859 van de Kreeke, J., and A. Hibma (2005), Observations on silt and sand transport in
 860 the throat section of the Frisian Inlet, *Coastal Engineering*, 52(2), 159–175, doi:
 861 10.1016/j.coastaleng.2004.10.002.
- 862 Van Der Hout, C. M., R. Witbaard, M. J. N. Bergman, G. C. A. Duineveld, M. J. C.
 863 Rozemeijer, and T. Gerkema (2017), The dynamics of suspended particulate
 864 matter (SPM) and chlorophyll- a from intratidal to annual time scales in a
 865 coastal turbidity maximum, *Journal of Sea Research*, 127(March), 105–118, doi:
 866 10.1016/j.seares.2017.04.011.
- 867 van der Werf, J., J. A. Á. Antolínez, L. Brakenhoff, M. Gawehn, K. den Heijer,
 868 H. de Loeff, R. Wilmink, M. van Maarseveen, H. Meijer-Holzhauer, J.-W. Mol,
 869 S. G. Pearson, B. van Prooijen, G. Santinelli, C. Schipper, M. Tissier, P. K. Tonnon,
 870 L. de Vet, T. Vermaas, R. J. Wilmink, and F. de Wit (2019), Datareport Kustgenese
 871 2.0., *Tech. Rep. 1220339-015-ZKS-0004*, Rijkswaterstaat, Delft, The Netherlands.
- 872 Van Prooijen, B. C., M. F. Tissier, F. P. De Wit, S. G. Pearson, L. B. Brakenhoff, M. C.
 873 Van Maarseveen, M. Van Der Vegt, J. W. Mol, F. Kok, H. Holzhauer, J. J. Van Der
 874 Werf, T. Vermaas, M. Gawehn, B. Grasmeyer, E. P. Elias, P. K. Tonnon, G. Santinelli,
 875 J. A. Antolínez, P. L. M. De Vet, A. J. Reniers, Z. B. Wang, C. Den Heijer, C. Van
 876 Gelder-Maas, R. J. Wilmink, C. A. Schipper, and H. De Loeff (2020), Measurements
 877 of hydrodynamics, sediment, morphology and benthos on Ameland ebb-tidal delta and
 878 lower shoreface, *Earth System Science Data*, 12(4), 2775–2786, doi:10.5194/essd-12-
 879 2775-2020.
- 880 Voulgaris, G., and S. T. Meyers (2004), Temporal variability of hydrodynamics, sediment
 881 concentration and sediment settling velocity in a tidal creek, *Continental Shelf Research*,
 882 24(15), 1659–1683, doi:10.1016/j.csr.2004.05.006.

- 883 Weeks, A. R., J. H. Simpson, and D. Bowers (1993), The relationship between concentra-
884 tions of suspended particulate material and tidal processes in the Irish Sea, *Continental*
885 *Shelf Research*, 13(12), 1325–1334, doi:10.1016/0278-4343(93)90086-D.
- 886 WET Labs Inc (2019), User manual: ECO Fluorometers and Scattering Sensors, *Tech.*
887 *rep.*, Philomath, OR.
- 888 WETLabs (2010), ECO 3-Measurement Sensor User’s Guide, *Tech. rep.*, WET Labs, Inc.,
889 Philomath, OR.
- 890 Winkelmolen, A. M., and H. J. Veenstra (1974), Size and shape sorting in a Dutch tidal
891 inlet, *Sedimentology*, 21(1), 107–126, doi:10.1111/j.1365-3091.1974.tb01784.x.
- 892 YSI Incorporated (2012), *6-Series Multiparameter Water Quality Sondes User Manual*, re-
893 vision j ed., 374 pp., YSI Incorporated, Yellow Springs, Ohio.
- 894 Zhu, Q., B. C. van Prooijen, D. C. Maan, Z. B. Wang, P. Yao, T. Daggars, and S. L.
895 Yang (2019), The heterogeneity of mudflat erodibility, *Geomorphology*, 345, doi:
896 10.1016/j.geomorph.2019.106834.